Cross-Coupling Coefficient Estimation of a Nano-g Accelerometer by Continuous Rotation Modulation on a Tilted Rate Table

Mengqi Zhang, Shitao Yan, Zhongguang Deng, Peng Chen, Zhi Li, Ji Fan, Huafeng Liu, Jinquan Liu, and Liangcheng Tu

***Abstract*— Nano-g accelerometers are widely used in space exploration and measurement of the earth's gravitational field. It is essential to precisely evaluate error effects at high orders such as cross-coupling for applications in a dynamic environment. Nevertheless, it remains challenging to meet the precision requirements using conventional calibration measures. In this article, we propose a method to separate the cross-coupling coefficients of a linear single-axis accelerometer by mounting it on a steadily rotating rate table that is tilted at a fixed deviation angle with respect to the horizontal plane. The gravity component is periodically modulated along the input axis per revolution. Simultaneously, a series of centripetal acceleration is applied along the cross axis in sequence while adjusting the rotation frequency of the rate table by steps. Thus, the cross-coupling coefficient can be separated by its dependence both on the modulated gravity acceleration and the centripetal acceleration. In comparison to the static multipoint angular rotation test on a tilted dividing head, the proposed dynamic modulation method demonstrates improved robustness against corruption from bias drift, with an improved uncertainty. This method to separate the cross-coupling coefficient is suitable for testing high-resolution accelerometers, without requiring high bias stability or sensitive response sustaining at ultralow frequency.**

***Index Terms*— Cross-coupling coefficient, model equation, nano-g accelerometer, parameter identification, rotation modulation, static multipoint.**

I. Introduction

ACCELEROMETERS with a resolution in the order of magnitude of ng/$\sqrt{\text{Hz}}$ (where $g \approx 9.8$ m/s^2 denotes the earth's gravity) are important for the exploration of temporal and spatial variations in gravitational field, providing information on the substance density distribution of our planet [1], [2]. The applications range from earth's crust movement through resource exploration to gravity-aided navigation [3], [4]. In many application scenarios like moving-base gravity measurements, accelerometers are required to resolve acceleration of nano-g or sub-nano-g in airborne or shipborne environments with relatively large dynamic noises [5], [6]. This requirement is demanding since the severe mechanical vibration of the moving vehicle can easily lead to corrupting effects through nonideal responses of accelerometers. For example, the principle of the commercial airborne gravity gradiometer is based on measuring the differences between matched pairs of rotating accelerometers. In such a gradiometer, second-order coefficients of a few $\mu g/g^2$ will produce a gradient bias error of many thousands of Eö (1 Eö $= 10^{-9}$ s^{-2}). This error due to response to base input accelerations is much greater than the desired resolution of $\sim$10 Eö. As another example, the electrostatic accelerometers with a sub-nano-g resolution in a narrow frequency band have been used in many space missions. The high-frequency vibrational disturbances could create spurious signals in the accelerometer measurement bandwidth through the second-order error coefficients, thus leading to the deteriorated accuracy of the electrostatic accelerometer, both in space and on ground [7]. For accelerometers generally used in space exploration, it is also known that ground-based calibration of the scale factor could present considerable uncertainty for on-orbit use [8]. This is due to the existence of 1-g gravity field on the ground, and error effects at the second order are among the potential sources. For such applications as mentioned above, it is desirable to perform detailed tests of accelerometers, to compensate for the error model coefficients, and finally to enhance the practical accuracy [9]–[12]. Therefore, it is valuable to investigate on the second-order effects including cross-coupling due to accelerations simultaneously applied along different axes.

The model equation of a linear single-axis, nongyroscopic accelerometer is normally treated as a mathematical series that relates the accelerometer output E to the components of acceleration along the reference axes [13]. Many procedures have been proposed for calibrating model terms of accelerometers. For accelerometers with a full-scale input range of about 1 g or a resolution no less than $\sim$1 μg, the local gravity field

Manuscript received February 2, 2021; revised March 9, 2021; accepted March 18, 2021. Date of publication April 19, 2021; date of current version April 23, 2021. This work was supported by the National Key Research and Development Program of China under Grant 2017YFC0601603. The Associate Editor coordinating the review process was Helko E. van den Brom. *(Corresponding author: Jinquan Liu.)*

Mengqi Zhang, Shitao Yan, Zhongguang Deng, Peng Chen, Zhi Li, Ji Fan, Huafeng Liu, and Jinquan Liu are with the MOE Key Laboratory of Fundamental Physical Quantities Measurement, Huazhong University of Science and Technology, Wuhan 430074, China, and also with the Hubei Key Laboratory of Gravitation and Quantum Physics, PGMF and School of Physics, Huazhong University of Science and Technology, Wuhan 430074, China (e-mail: jinquanliu@hust.edu.cn).

Liangcheng Tu is with the MOE Key Laboratory of Fundamental Physical Quantities Measurement, Huazhong University of Science and Technology, Wuhan 430074, China, also with the Hubei Key Laboratory of Gravitation and Quantum Physics, PGMF and School of Physics, Huazhong University of Science and Technology, Wuhan 430074, China, also with the TianQin Research Center for Gravitational Physics, Sun Yat-sen University (Zhuhai Campus), Zhuhai 519082, China, and also with the School of Physics and Astronomy, Sun Yat-sen University (Zhuhai Campus), Zhuhai 519082, China.

Digital Object Identifier 10.1109/TIM.2021.3070601

test such as multipoint methods are conventionally available for determining the accelerometers' linear, nonlinearity and cross-coupling coefficients based on a dividing head [14]–[17]. For accelerometers with a full-scale input larger than 1 g, a precision centrifuge is often used to precisely produce acceleration with the required magnitude [18]–[21]. Dynamic tests are generally carried out on an electromagnetic vibrator [22]–[24]. Various accelerometer orientations and their combination are designed to excite the target model terms on these two types of equipment and then separate the coefficients [13], [25]. The input acceleration typically ranges from submilli-g to tens of g. However, the above procedures are not qualified anymore for testing accelerometers with a resolution of nano-g. The challenges come from several possible reasons. First, the full-scale input of nano-g accelerometers is typically a couple of milli-g, far below 1 g. The existing methods like exciting nonlinearity effects on a centrifuge [26] are not feasible anymore because both the equipment and procedures are usually not dedicated to stringent test requiring nano-g precision. Second, precise calibration is subjected to disturbances from the test environment which is typically much higher than 1 n$g/\sqrt{\text{Hz}}$ over 0.1 Hz. In addition, accelerometers optimized for dynamic performance are not necessarily equipped with long-term stability of bias or excellent response at ultralow frequency. For example, the accelerometer dedicated to the use in a rotating accelerometer gravity gradiometer emphasizes dynamic performance more than bias stability because the gravity gradient signal is modulated onto twice the rotation frequency of ~0.25 Hz [27]; many commercial seismometers are able to resolve acceleration of ~1 n$g/\sqrt{\text{Hz}}$, but insensitive to excitation at ultralow frequency [28]. This practical issue imposes constraints on the use of static measurements such as static multipoint tumbling accelerometers on a dividing head. To date, a few literatures have been published to investigate the nonlinearity response of accelerometers or seismometers which are sensitive to excitation of nano-g acceleration. For example, the quadratic term of the ultrasensitive space accelerometers with a higher resolution than nano-g was identified and compensated using an iterative calibration method, by comparing the accelerometer response within the measurement bandwidth with and without the high-frequency signal [7], [29], [30]. As for seismometers, nonlinearity distortion was measured on a shake table by exciting the table with two-tone signals at various frequencies [28]. These studies have concentrated on the second-order nonlinearity response to acceleration along the input axis (IA). Among the second-order effects, the cross-coupling between acceleration along the IA and the cross axis is frequently considered to be as important as nonlinearity response to the IA. However, the procedure for separating these cross-coupling coefficients of nano-g accelerometers is yet to be elucidated.

In this article, we proposed a new method to evaluate the cross-coupling effects of single-axis nano-g accelerometers. The accelerometer is mounted on a steadily rotating rate table tilted with a fixed deviation angle from the horizontal plane and its IA is tangential to the circumference of the rate table; thus, the input acceleration is modulated at the rotation frequency with respect to gravity. By adjusting the rotation frequency in steps, the centripetal acceleration is sequentially changed. Then, the cross-coupling coefficients are separated by the output correlation both with the modulated input acceleration in the gravity field and with the rotation frequency. The possible error sources are systematically investigated and analyzed. In addition to the test by the proposed method, a homemade accelerometer [31] was also tested for comparison with a method of 12 points discrete angular rotation on a tilted dividing head.

II. Model

In this section, the model equation of the linear single-axis, nongyroscopic accelerometer is given at first. Subsequently, the conventional multipoint test on a tilted dividing head is briefly introduced for calibration of the cross-coupling coefficients. Based on the introduction, the rotation modulation method is developed to rotate the accelerometer on a precision single-axis rate table tilted at a small angle.

A. Output Model of Accelerometer

The output of the accelerometer is defined as a simplified series that mathematically relates the accelerometer output to the components of applied acceleration [13]. Neglecting the angular movement and asymmetry terms, the accelerometer's output (E, volts in this article) is given by

$$E = K_1\big(K_0 + a_\mathrm{i} + K_2 a_\mathrm{i}^2 + K_\mathrm{ip} a_\mathrm{i} a_\mathrm{p} + K_\mathrm{io} a_\mathrm{i} a_\mathrm{o} + K_\mathrm{po} a_\mathrm{p} a_\mathrm{o} + K_\mathrm{oo} a_\mathrm{o}^2 + K_\mathrm{pp} a_\mathrm{p}^2 + \delta_\mathrm{o} a_\mathrm{p} - \delta_\mathrm{p} a_\mathrm{o} + \varepsilon\big) \quad (1)$$

where

K_0, K_1, K_2 bias (g), the scale factor (V/g), and the second-order coefficient (g/g^2), respectively;

a_i, a_p, a_o applied acceleration components along the IA, pendulum axis (PA), and output axis (OA) (g), respectively;

K_ip, K_io, K_po cross-coupling coefficients (g/g^2);

K_oo, K_pp second-order output cross-axis nonlinearity coefficient and the second-order pendulous cross-axis nonlinearity coefficient (g/g^2), respectively;

δ_o, δ_p misalignment of the IA with respect to the input reference axis about the OA and PA, respectively (rad);

ε measurement and process noise and unmodeled error (g).

B. Determination of Cross-Coupling Coefficients on a Conventional Dividing Head

The conventional static multipoint test is typically implemented by tumbling the accelerometer with its IA perpendicular to the horizontal rotation axis of the dividing head in a 1-g gravity field. This method is not directly applicable to the test of nano-g accelerometers with a full-scale input far below 1 g. In IEEE Std 836 [25], a method is described to measure the transfer function of an accelerometer in the low-frequency range, making use of a rate table with its spin axis tilted in the gravity field. The dual-axis tilt method, performed on a tilted dividing head, was applied to the resolution test of accelerometers in some cases [32]. Here, these methods are extended to estimate the cross-coupling coefficients of the nano-g accelerometer. As shown in Fig. 1,

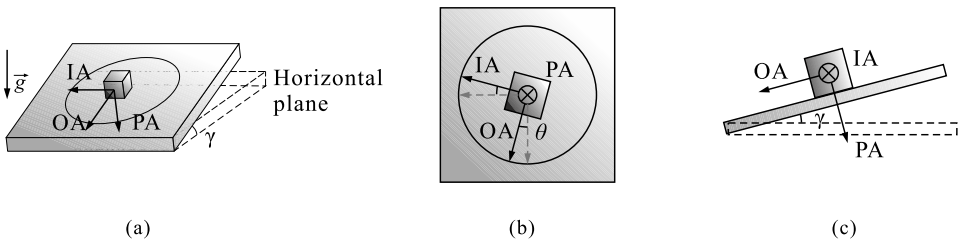

Fig. 1. Schematic mounting configurations of the accelerometer on the dividing head. (a) Pictorial diagram. (b) Plan view. (c) Side view. The IA and OA of the accelerometers are parallel to the mounting surface.

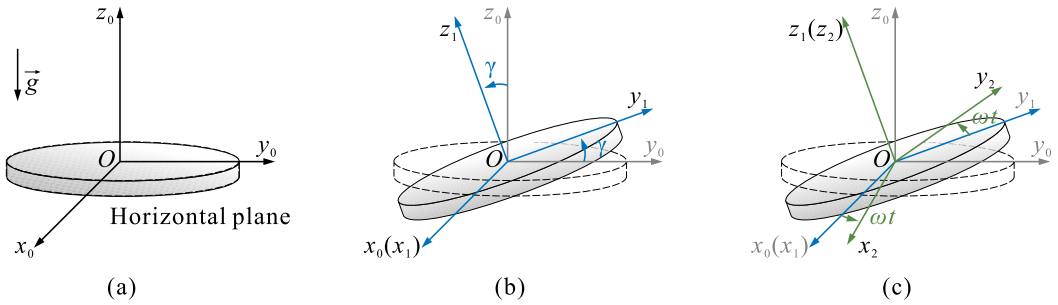

Fig. 2. Schematic of the precision single-axis rate table and coordinate systems (a) initial coordinate, (b) coordinate tilted to γ relative to the initial coordinate, and (c) coordinate rotating about the Oz_1-axis at an angular velocity ω.

the IA of the accelerometer is parallel to the mounting surface of a dividing head, and the OA is chosen to be within the mounting surface while the PA is normal to the mounting surface. Then, the dividing head provides variable acceleration by rotating on a tilted plane to a sequence of angles with uniform angle spacing within 360°. Note that it is taken as an example how to calibrate K_{io}. The other cross-coupling coefficient K_{ip} can also be measured by simply flipping the PA and the OA. Those coefficients of model terms can be obtained by least-squares fitting or harmonic analysis of the data measured at multipositions [13]. The accuracy of this static method is susceptible to environmental tilt variations, equipment accuracy, and the accelerometer bias drift in the test duration.

C. Determination of Cross-Coupling Coefficients by the Rotation Modulation Method on a Tilted Precision Single-Axis Rate Table

In this article, a novel scheme is developed to improve the calibration accuracy of cross-coupling coefficients for our home-made nano-g accelerometer. A tilted precision single-axis rate table is used in this method. As shown in Fig. 2(a), the initial coordinate system of the rate table is defined as $Ox_0y_0z_0$. This system is fixed relative to the laboratory, and the x_0 Oy_0 plane is horizontal. Then, a gravity component is provided with the rate table tilted about the Ox_0-axis by a small angle γ, as illustrated in Fig. 2(b). The IA of the accelerometer is parallel to the rate table's top. A new stationary coordinate system $Ox_1y_1z_1$ is defined here, where the x_1Oy_1 plane is parallel to the tilted rate table. In the test, the rate table rotates about its spin axis (Oz_1-axis) at an angular velocity ω, as shown in Fig. 2(c). Here, a rotating coordinate system $Ox_2y_2z_2$ is defined, moving together with the accelerometer.

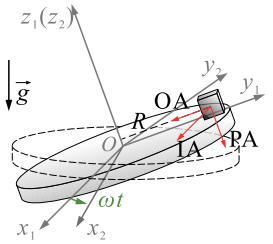

Fig. 3. Side view of the precision single-axis rate table.

As shown in Fig. 3, the accelerometer under test is installed on a circular rotation fixture and located at a distance R away from the spin axis, with its IA along the Ox_2-axis (initially parallel to the Ox_1-axis) and the OA along the Oy_2-axis (initially parallel to the Oy_1-axis). Then, the centripetal acceleration $\omega^2 R$ will be imposed onto the OA, when the rate table rotates at a steady angular velocity ω. During rotation, the two gravity components along the IA and the OA will be periodically modulated, with their phases orthogonal to each other.

The acceleration produced by gravity is $[0\ 0\ g]^{\text{T}}$ in the $Ox_0y_0z_0$. Given the tilt angle γ of the rate table, the acceleration in the $Ox_1y_1z_1$ is expressed as follows:

$$\begin{bmatrix} g_{x1} \\ g_{y1} \\ g_{z1} \end{bmatrix} = \begin{bmatrix} 1 & 0 & 0 \\ 0 & \cos\gamma & \sin\gamma \\ 0 & -\sin\gamma & \cos\gamma \end{bmatrix} \begin{bmatrix} 0 \\ 0 \\ g \end{bmatrix}. \tag{2}$$

Along with time increase, the rate table revolves about the Oz_2-axis with ω. The gravity acceleration applied onto the IA, the OA, and the PA is denoted as a_{ig}, a_{og}, and a_{pg}, respectively. Assuming that the Oy_2-axis is overlapped with the Oy_1-axis at $t = 0$, the gravity components with respect to the initial state

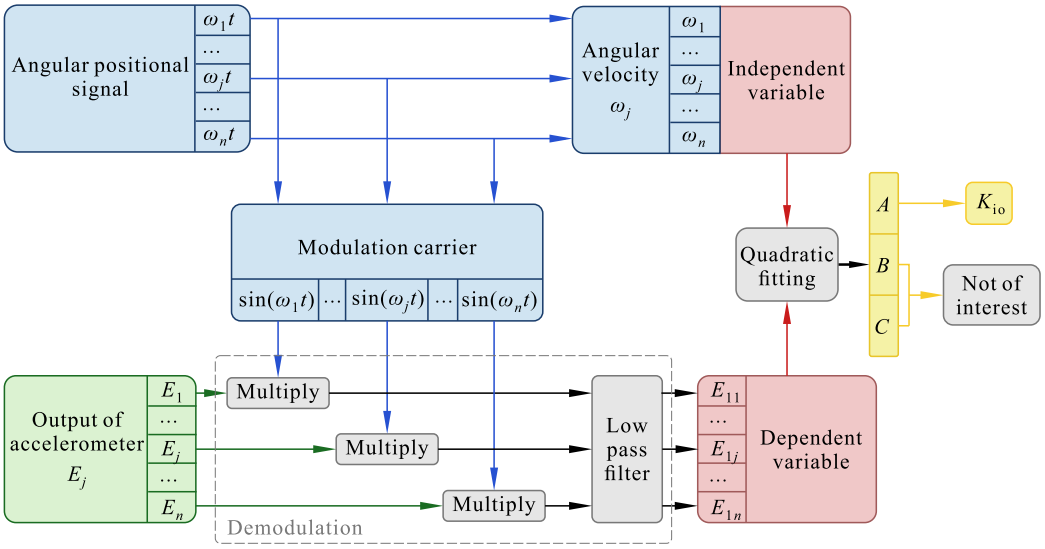

Fig. 4. Flowchart for separating K_{io}, where the angular velocity is the derivative of the angular position signal which is produced by the grating of the rate table. A, B, and C are the coefficients of the quadratic fitting, where only A is associated with K_{io} of interest.

are

$$\begin{bmatrix} a_{ig} \\ a_{og} \\ a_{pg} \end{bmatrix} = \begin{bmatrix} \cos\omega t & \sin\omega t & 0 \\ -\sin\omega t & \cos\omega t & 0 \\ 0 & 0 & 1 \end{bmatrix} \begin{bmatrix} g_{x1} \\ g_{y1} \\ g_{z1} \end{bmatrix} = \begin{bmatrix} g\sin\gamma\ \sin\omega t \\ g\sin\gamma\ \cos\omega t \\ g\cos\gamma \end{bmatrix}. \tag{3}$$

Simultaneously, the centripetal acceleration $\omega^2 R$ is applied onto the OA as well. The centripetal acceleration components $a_{i\omega}$, $a_{o\omega}$, and $a_{p\omega}$ along the three axes of the accelerometer are expressed as

$$\begin{bmatrix} a_{i\omega} \\ a_{o\omega} \\ a_{p\omega} \end{bmatrix} = \begin{bmatrix} 0 \\ \omega^2 R \\ 0 \end{bmatrix}. \tag{4}$$

Considering the combined effects of gravitational and centripetal acceleration, the overall acceleration components are

$$\begin{bmatrix} a_i \\ a_o \\ a_p \end{bmatrix} = \begin{bmatrix} a_{ig} \\ a_{og} \\ a_{pg} \end{bmatrix} + \begin{bmatrix} a_{i\omega} \\ a_{o\omega} \\ a_{p\omega} \end{bmatrix} = \begin{bmatrix} g\sin\gamma\ \sin\omega t \\ g\sin\gamma\ \cos\omega t + \omega^2 R \\ g\cos\gamma \end{bmatrix}. \tag{5}$$

Substituting (5) into (1), the calculated output of the tested accelerometers is expressed as follows:

$$\begin{aligned} \frac{E}{K_1} &= K_0 + K_{po} g\omega^2 R\cos\gamma + K_{oo}\omega^4 R^2 + K_{pp} g^2\cos^2\gamma \\ &\quad + \delta_o g\cos\gamma - \delta_p \omega^2 R + 0.5K_2 g^2\sin^2\gamma \\ &\quad + 0.5K_{oo} g^2\sin^2\gamma + \cos\omega t \\ &\quad \times \left(K_{po} g^2\sin\gamma\cos\gamma + 2K_{oo} g\omega^2 R\sin\gamma - \delta_p g\sin\gamma\right) \\ &\quad + \underline{\sin\omega t}\left(\underline{K_{io} g\omega^2 R\sin\gamma} + g\sin\gamma + K_{ip} g^2\sin\gamma\cos\gamma\right) \\ &\quad + \sin 2\omega t\left(0.5K_{io} g^2\sin^2\gamma\right) \\ &\quad + \cos 2\omega t\left(-0.5K_2 g^2\sin^2\gamma + 0.5K_{oo} g^2\sin^2\gamma\right) + \varepsilon. \end{aligned} \tag{6}$$

In (6), there exists one double-underlined unique term where K_{io} is associated with both $\sin\omega t$ and ω^2. Based on this characteristic, we can identify K_{io}, by demodulating the output at $\sin\omega t$ and then fitting with quadratic dependence on ω. The phase of the modulation carrier is produced by the synchronous angular position signal of the circular grating of the rate table with an accuracy of $1''$, relative to the initial angular position (the Oy_1-axis) as shown in Fig. 2(b).

As shown in Fig. 4, K_{io} is separated according to the following process: the output E_j of the accelerometer is collected in sequence at a series of chosen ω's, denoted as ω_j, $j = 1, \ldots, n$; the output E_j is then demodulated by multiplying with $\sin\omega_j t$, and then converted into $E_{1\,j}$ including all underlined terms following behind $\sin\omega_j t$ in (6) after a low-pass filter; subsequently, the set of $E_{1\,j}$ is fitted as a function of ω_j by a quadratic polynomial; and ultimately, the coefficient of the quadratic term is used to deduce K_{io}.

The quadratic polynomial is written as

$$\frac{E_{1j}}{K_1} = A\omega_j^2 + B\omega_j + C \tag{7}$$

where A, B, and C are the fitting coefficients, and A is equal to $K_{io} R g \sin\gamma$. Among all the terms included in $E_{1\,j}$, only the second-order coefficient A containing K_{io} is of our interest. Ultimately, K_{io} could be deduced since all other factors in A are known including R, g, and γ. In (7), the term $B\omega_j$ is introduced to take into account some unwanted effects.

III. Experimental Configurations, Experimental Preparations, and Error Evaluation

The test has been carried out on a test pier in a cave laboratory to alleviate the disturbance of cultural electromagnetic and seismic noise. The laboratory is located at Wuhan, with a north latitude of 30.5° and an east longitude of 114.4°. The effects of cross-coupling are usually several μg or less for nano-g accelerometers while strongly excited but still kept in

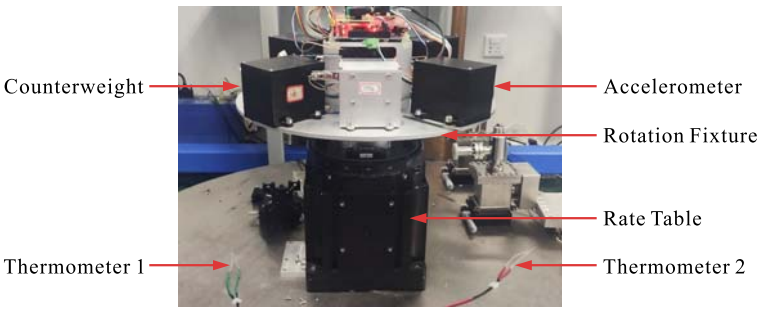

Fig. 5. Accelerometers mounted on the rotation fixture of the precision single-axis rate table. Two thermometers are deployed at opposite sides of the rate table.

normal operation. To separate the cross-coupling coefficients, potential error sources need to be systematically analyzed if their effects could reach tens of ng. At first, accelerometers must be accurately mounted with the required position and orientations. Second, it must be ensured that the accelerometer output is demodulated in phase with the modulation carrier. Third, potential issues such as temperature fluctuation and base tilt variations need to be addressed. Fourth, the movement imperfections of the rate table are essential for performance of the procedure, even though the rate table and the rotation controller are optimized for stable rotation movement. Finally, the accelerometer could respond differently under excitation at different frequencies. This effect needs careful treatment especially when we are exploring the cross-coupling effects based on varying rotation frequency.

A. Test Configurations on the Rate Table

A home-made accelerometer is mounted on the fixture at the top of the rate table as shown in Fig. 5. The rate table features excellent speed stability of 1 part per million (ppm) per revolution and wobble of the spin axis less than $1''$. The spin axis is normal to the surface of the rotation fixture within $\pm 1''$.

In the test, the acceleration along the IA and the OA should be maximized while keeping accelerometer output safely within its output range, to enhance the cross-coupling effect. The accelerometer under test has an input range of ± 5 mg with a scale factor of 566.2 V/g, which has been determined on the dividing head with an angular accuracy of $1''$. Based on these considerations, the tilt angle is set to be $(360 \pm 7)''$ in virtue of an electronic level meter with an accuracy of $0.1''$ in the horizontal state and $7''$ at a tilt of $360''$, corresponding to acceleration of 1.8 mg applied onto the IA.

The rate table is optimized for steady rotation within a spin frequency range from 0.09 to 0.25 Hz, corresponding to an angular velocity from $9\pi/50$ to $\pi/2$ rad/s. The accelerometers are located 10 cm away from the spin axis with an uncertainty of 1 mm, which will introduce an error of $\pm 1\%$ to K_{io}. Taking both the rotation angular velocity and the radius into account, the centripetal acceleration ranges from 3 to 25 mg along the OA.

In our test, the PA is defined to be normal to the bottom surface of our accelerometer. According to this definition, the direction of the PA could be ensured to be normal to the fixture surface with an uncertainty of $1''$ by mounting the accelerometer with its case bottom in rigid contact with the fixture. The IA is defined to be along the tangential orientation of the fixture circumference and the OA along the radius. When the rate table rotates at different spin frequencies, the dc output component of the accelerometer changes due to its cross-axis sensitivity to the centripetal acceleration. Based on this effect, we have minimized the dc output variations by slightly adjusting the accelerometer orientation along the fixture top surface within the tolerance of the retaining holes when switching spin frequencies. Since the accelerometer under test stably distinguishes a dc output change of ~ 5 μg, the IA is under control with an uncertainty better than 0.2 mrad using a centripetal acceleration of 25 mg. Once the PA and the IA are determined, the orientation of the OA is fixed, because it is defined to be normal to both. According to this mounting procedure, the realized axis orientation could slightly deviate from the ideal coordinate system $Ox_2y_2z_2$ in Fig. 3. The deviation could lead to mixing between terms in (1). To evaluate the mixing between secondary error terms, a multipoint test on the tilted dividing head has been performed at first. The test results show that the cross-coupling or nonlinearity coefficients of our accelerometer are no larger than 0.2 g/g^2 at maximum. Then, a further analysis is carried out according to (1) based on coordinate transformations and the orientation uncertainties, indicating that the relative uncertainty of K_{io} is no more than 1‰. Note that the IA misalignment δ_{p} about the PA is minimized in this way with an uncertainty of 0.2 mrad. The advantage of minimizing δ_{p} is to avoid large output variations through cross-axis sensitivity to the relatively wide range of centripetal acceleration in our test.

While the rate table rotates, the accelerometer senses the Coriolis acceleration produced by earth's rotation and the tangential velocity $R\omega_j$. Earth's rotation could be decomposed into components along the mounting surface and its normal line (overlapped with the spin axis of the table within $\pm 1''$, as mentioned before). By interacting with the tangential velocity, the component along the normal line leads to an acceleration a_{oc} along the OA, which is

$$a_{\text{oc}} = 2\omega_j R\omega_{\text{e}} \sin\psi \tag{8}$$

where ω_{e} is the angular velocity of earth's rotation and ψ is the angle between the normal line and the equatorial plane. The tilt angle of the fixture is negligibly small from the local

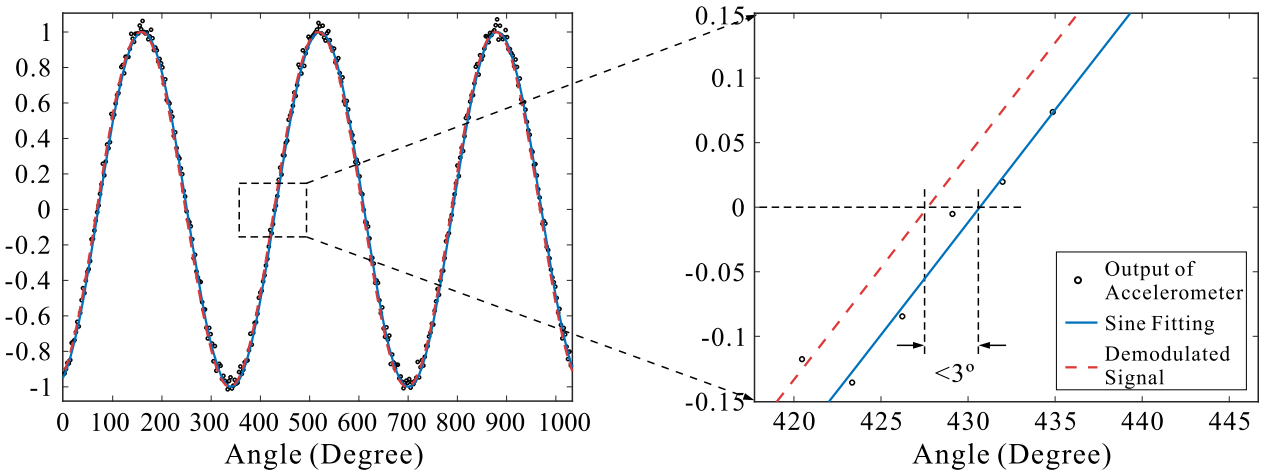

Fig. 6. Phase alignment between the normalized modulation carrier and the output of the accelerometer at an angular velocity of $\pi/2$ rad/s, respectively, represented by the red dashed curve and black circles. The blue curve represents the sine fit of the output signal.

horizontal, compared with the latitude of the experimental site (360″ versus 30.5°). Therefore, the latitude is taken as the approximate value of ψ. Accordingly, the Coriolis acceleration component is about 1.1 μg at maximum, while the centripetal acceleration applied in the experiment is 3–25 mg. The latter is at least three orders of magnitude larger than the former.

The other component of earth's rotation along the mounting surface leads to acceleration a_{pc} along the PA, which is

$$a_{\mathrm{pc}} = 2\omega_j R\omega_{\mathrm{e}} \cos\psi \sin\left(\omega t + \varphi_{\mathrm{p0}}\right) \tag{9}$$

where φ_{p0} is the compensation phase for a_{p} relative to the initial angular position of the accelerometer. This term is below 2 μg. Unlike the centripetal acceleration $a_{\mathrm{o}\omega}$ with a quadratic relation to ω_j, both Coriolis acceleration components a_{oc} and a_{pc} instead have a linear relation to ω_j. Therefore, the Coriolis acceleration finally goes into the linear term $B\omega_j$ in (7) via cross-sensitivity or cross-coupling, which is of no interest. To summarize, the Coriolis acceleration can be ignored in this work.

B. Phase Alignment of Demodulation and Data Collection Time

As mentioned above, the rate table rotates at variable discrete angular velocities. The output of the accelerometer needs to be demodulated with the sinusoidal wave $\sin\omega_j t$, as the first step of separating the cross-coupling coefficient shown in Fig. 4. In our test, the accelerometer output should be aligned in phase with the modulation carrier, satisfying the assumption of (3). In case that the output signal should possess a phase error φ_0 relative to the modulation carrier, the demodulation result according to (6) would contain the following terms:

$$\begin{aligned} &K_{\mathrm{io}} g\omega^2 R \sin\gamma \cos\varphi_0 + K_{\mathrm{oo}} g\omega^2 R \sin\gamma \sin\varphi_0 + \cdots \\ &\quad = gR\sin\gamma\left(K_{\mathrm{io}}\cos\varphi_0 + K_{\mathrm{oo}}\sin\varphi_0\right)\omega^2 + \cdots . \end{aligned} \tag{10}$$

It can be seen that the magnitude of K_{io} will be reduced by a factor of $\cos\varphi_0$ and will be mixed with another coefficient K_{oo} by coupling through $\sin\varphi_0$.

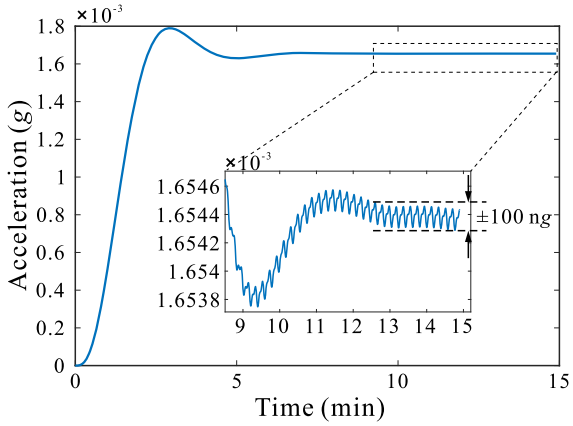

Fig. 7. Time response of the demodulated signal after narrow-bandwidth filtering. The magnified inset shows that the filtered output is stabilized within ±100 ng after ∼12 min.

To evaluate the phase alignment, the accelerometer output E_j and the modulation carrier $\sin(\omega_j t+\varphi_0)$ are simultaneously monitored. The initial phase φ_0 of the modulation carrier is adjusted until the phase difference between the two is acceptable. As shown by the experimental data plotted in Fig. 6, the phase difference between the red dashed line representing the modulation carrier and the blue line representing the accelerometer output reaches less than 3°. With a phase error of 3°, the absolute value of K_{io} decreases by 1‰ due to the factor $\cos\varphi_0$. Since K_{oo} is much smaller than K_{io} in our case and $\sin\varphi_0$ is much less than 1, the second term K_{oo} $\sin\varphi_0$ of their product is negligible. It is worthy of mentioning that the misalignment δ_{p} about the PA could introduce a phase error through cross-sensitivity to the gravity component along the OA. However, uncertainty of 0.2 mrad is negligible. The misalignment δ_{o} only introduces a static error and has no influence on the phase alignment. The error effects at the second-order are estimated to be ignorable on the phase alignment, as well.

To suppress the noise, a low-pass filter with a narrow bandwidth for demodulation is adopted to improve the signal-to-noise ratio. As shown in Fig. 7, the demodulation output

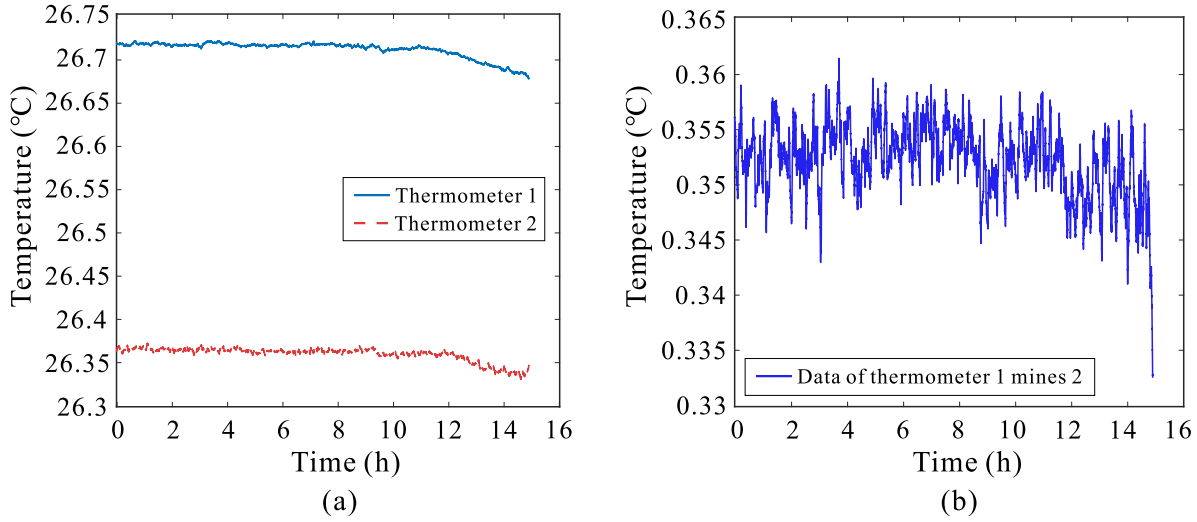

Fig. 8. Temperature variations within 16 h when thermometers 1 and 2 were fixed on opposite sides of the rate table as shown in Fig. 5. (a) Temperatures on either side of the rate table. (b) Difference between the output of thermometer 1 and thermometer 2.

tends to converge and stabilize within ±100 n*g* after the initial oscillation fades out in 12 min. In addition, when switching between spin frequencies, a few minutes are necessary for the rate table to reach rotation stability of 1 ppm per revolution. Based on the considerations mentioned above, a duration of 15 min is chosen for testing at each rotation frequency. In one complete set of tests, there are nine discrete spin frequencies sequentially scheduled in total, ranging from 0.09 to 0.25 Hz with an interval of 0.02 Hz. Thus, one set of tests last ∼2.25 h. The test at each frequency in the set is sequentially carried out and then analyzed, according to the flowchart shown in Fig. 4.

C. Tilt Drift of Test Equipment and Temperature Drift

Since a full set of test lasts more than 2 h, one should pay particular attention to influences which cause tilt drift of the spin axis in the test duration. The tilt drift goes directly into acceleration along the IA in the form of the tilt-related gravity component. Hence, time-varying tilt drift could be simply misinterpreted as cross-coupling effects arising from sequentially switching the spin frequency between tests.

The test base, including the fixture, the rate table, and the pier, could be thermally deformed in the presence of a temperature gradient. Further analysis, however, tells that a constant temperature gradient is not disturbing as long as unchanged deformation has been taken in as one part of the measured tilt angle. It is the uncontrolled time variation in the tilt angle which could interfere with the test. As shown in Fig. 5, the temperature around the rate table was monitored for about 16 h using two thermometers with a resolution of 1 mK. The thermometers were deployed at opposite sides of the rate table with a distance of ∼40 cm, named thermometer 1 and thermometer 2, respectively. During the whole process, the ambient temperature fluctuates within ±0.01 °C/h, as shown in Fig. 8(a). The temperature difference in thermometers is kept constant at ∼0.35 °C, which is reconfirmed to be real by exchanging the position of two thermometers. To evaluate the drift of the temperature gradient, each set

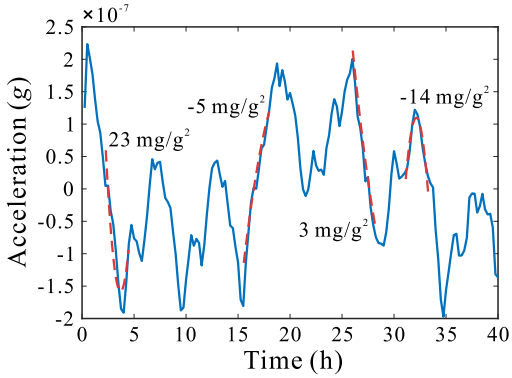

Fig. 9. Output of the accelerometer at a fixed spin frequency due to tilt drift. The red dashed curve represents continuous data segment randomly selected with a duration of 2.25 h, whose error contribution to K_{io} is marked.

of the experimental data is subtracted by its mean value. As shown in Fig. 8(b), the temperature consistently follows the same tendency within 0.01 °C. This brings out a temperature gradient drift less than 0.01 °C per 40 cm. Based on the thermal expansion coefficients and the dimensions of the test equipment, the drift of the temperature gradient is estimated to produce a tilt variation below 50 nrad.

The temperature sensitivity of the scale factor of the accelerometer has been measured to be less than 450 ppm/°C, which will result in an acceleration error of ±20 n*g* in a single set of tests lasting 2.25 h with the temperature drift rate of ∼ ±0.01 °C/h. The temperature of the test site is kept at 26.5 °C with an uncertainty of 0.2 °C from day to day, resulting in a negligible error of ±0.1‰ among different sets.

When the ambient temperature was kept properly stable at such a level, the output drift of the accelerometer was monitored for 40 h at a fixed rotation frequency for the sake of evaluating the tilt drift when the table was in movement. As shown in Fig. 9, the accelerometer output at a fixed rotation speed illustrates a fluctuation of ±200 n*g*, which corresponds to a tilt drift of approximately ±200 nrad for an accelerometer with its IA in the horizontal plane. As mentioned above,

the effects of temperature and temperature gradient are only accountable for variations about 50 ng and insufficient to justify such large fluctuation here. Eventually, it is inferred that the dominant sources come from slow drift of the spin axis due to the time-varying inclination of the test pier and the imperfect bearings of the rate table. Although the cave laboratory provides an environment already seismically isolated from urban noise, there still exists the tidal tilt effect which could be as large as ±160 nrad (about ±160 ng) [33]. More than that, if the tidal tilt was the only dominant factor, its effect could be corrected to a large extent using the tidal tilt record in the same laboratory in principle. However, detailed analysis of Fig. 9 tells that there is another influential factor, which we attribute to the long-term irregular wobble movement of the spin axis. Actually, the disadvantageous influence of wobble is already greatly suppressed from its nominal value of 1″ by averaging over many turns in virtue of narrow-bandwidth filtering, but there still remains a small portion of wobbling movement about 200 nrad which is unrepeatable. The irregular wobble contributes together with the tidal tilt to orientation of the spin axis, resulting in an unpredictable tilt drift.

We mimic the possible tilt drift by randomly pulling out any continuous data segment of 2.25 h from this long sequence of data as shown in Fig. 9, to evaluate the fake effects. It should be noted that the spin frequency is kept constant here on purpose so that only tilt drift takes effects and other effects such as cross-coupling do not change over time. Subsequently, nine average tilt angles are deduced by sequentially averaging over data fragments every 15 min with spacing in-between them, mimicking one set of tests. In such a way, we take the gravity components related to nine average tilt angles as the sole input to the accelerometer. Finally, the set of nine gravity components corresponding to tilt angles are fitted as a function of ω_j by a quadratic polynomial and a fake K_{io} is derived according to (7). When the same procedure is applied to many segments, the disturbing effect of the tilt drift could be statistically evaluated. As shown by the red dashed line in Fig. 9, the fitting results of K_{io} are given for four representative segments. These added errors by tilt drift are dispersed and could be as large as ±30 mg/g^2 at maximum.

D. Rotation Velocity Stability of the Rate Table

Although the precision single-axis rate table is dedicated to continuous steady rotation, unfavorable rotation noises still occur at a very high precision level. Especially, periodic spin imperfection results in tangential acceleration at harmonics, which is directly applied along the IA and might confusingly show the same dependence on rotation as the cross-coupling effect. The angular movement can be simply expressed in relation to position-related rotation imperfection as

$$\varphi = \omega_j t + \theta_1 \sin\left(\omega_j t + \varphi_1\right) + \theta_2 \sin\left(2\omega_j t + \varphi_2\right) + \cdots \quad (11)$$

where θ_1 and θ_2 are, respectively, the amplitude of the first harmonic and that of the second harmonic, and φ_1 and φ_2 are the corresponding phases. Take the second derivative of (11) and multiply it by the radius R, and then the rotation-related tangential acceleration $a_{\varphi j}$ is deduced as

$$a_{\varphi j} = -R\omega_j^2\theta_1 \sin\left(\omega_j t + \varphi_1\right) - 4R\omega_j^2\theta_2 \sin\left(2\omega_j t + \varphi_2\right) + \cdots . \quad (12)$$

It can be seen that the term $R\omega_j^2\theta_1 \sin(\omega_j t + \varphi_1)$ presents the same dependence on $\sin\omega_j t$ and ω_j^2 as the K_{io} term of our interest in (6). To evaluate the disturbance caused by the rotation velocity imperfection, we monitor the angular velocity of the rate table using an optic fiber gyroscope with bias stability ≤0.002°/h and angle random walk ≤0.001°/$\sqrt{\text{h}}$. The rotation-related tangential acceleration is the product of the radius R and the derivative of the angular velocity. We take the rotation-related acceleration at different spin frequencies as the only input to the accelerometers and mimic one set of tests. After the input acceleration is demodulated with the sine wave at the respective frequencies, the acceleration amplitude is derived. The amplitude of the rotation-related tangential acceleration is depicted as a function of the spin frequencies in Fig. 10. It is noted that the rotation-related tangential acceleration at the first harmonic indeed correlates with the rotation frequency. Equation (7) is used to fit the demodulated amplitude across the frequency range. The fitting result is given by

$$a_{\varphi j} = 7(\pm 24) \times 10^{-7}\left(\frac{\omega_j}{2\pi}\right)^2 + 3(\pm 8) \times 10^{-7}\frac{\omega_j}{2\pi} - 2(\pm 7) \times 10^{-8} \quad (13)$$

where $a_{\varphi j}$ is the tangential acceleration of the rate table and ω_j is the rotation angular velocity. Therefore, it is deduced that the rotation speed instability gives an error of (1 ± 3) mg/g^2 for K_{io}.

E. Response of the Accelerometer in Relation to Input Acceleration Frequencies

When the spin frequency of the rate table is changed, the output of the accelerometer could change simply because of its scale factor dependence on the input acceleration frequency. This frequency-dependent response could be easily mistaken as the consequence of cross-coupling arising from

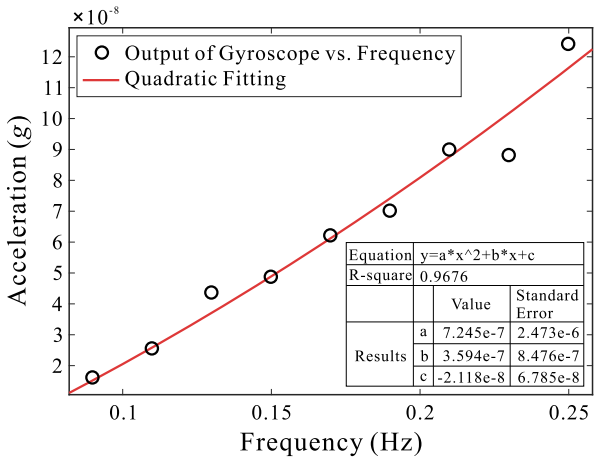

Fig. 10. Amplitude of rotation-related tangential acceleration in relation to rotation frequencies. The black circles represent the acceleration derived from the gyroscope output, and the red curve is the fitting curve according to (7).

TABLE I
CONTRIBUTION TO K_{io} OF ALL ERROR SOURCES

Error sources		Uncertainty	Contribution to K_{io}
Tilt angle deviation		7″	±2%
Radius		1 mm	±1%
Orientation of cross axes	PA	1″	±0.9 μg/g^2
	OA	0.2 mrad	±40 μg/g^2
Phase alignment of demodulation		3°	−1‰
Temperature influence on scale factor		9ppm	± 0.1 mg/g^2
Tilt drift of test equipment		200 nrad	±30 mg/g^2
Rotation velocity stability of rate table			1±3mg/g^2
Accelerometer response on frequency		0.2‰	0.8±2.6 mg/g^2

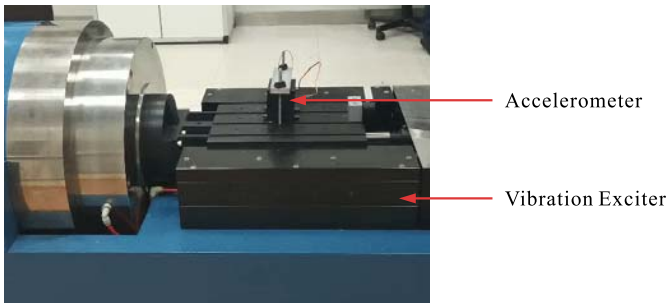

Fig. 11. Ultralow frequency vibration calibration system with the accelerometer mounted on its rail.

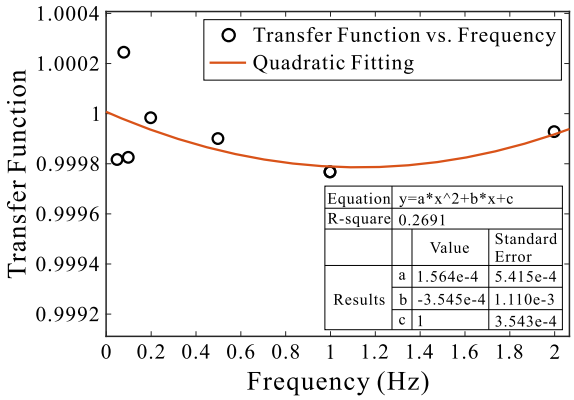

Fig. 12. Response of the accelerometer between 0.09 and 2 Hz.

rotation-related centripetal acceleration variation along the OA. The accelerometer has been excited by frequency sweep conforming to the ISO 16063-11 on an ultralow frequency vibration calibration system with gas bearing developed by the Institute of Manufacturing Technology and Automation, Zhejiang University, Hangzhou, China, as shown in Fig. 11. The response of the accelerometer is shown as a function of excitation frequency in Fig. 12, from 0.09 to 2 Hz. The response presents good consistency within ±0.2‰ at different frequencies. The response in this frequency range is expected to be flat for our accelerometer with a bandwidth larger than 10 Hz. This response curve is fitted with (7) to find the quadratic relationship with ω_j. The result indicates that there is no significant square or linear relation between the accelerometer response and the frequency. Given that the modulation amplitude of the gravity component along the IA is 1.8 mg, the frequency response inconsistency corresponds to a potential K_{io} error of (0.8 ± 2.6) mg/g^2.

Based on the above analysis, all errors that may affect the separation of K_{io} are estimated. The major effects of different sources are summarized in Table I. The dominant error is from the spin axis tilt drift relative to the local plumb line, which is ±30 mg/g^2 at maximum.

IV. EXPERIMENTAL RESULTS OF CROSS-COUPLING DETERMINATION AND ANALYSES

Varying rotation-frequency experiments were carried out on a tilted rate table, and then data were processed according to the flowchart in Fig. 4. As shown in Fig. 13(a), the results of three sets of tests are plotted as examples. The demodulated output of the accelerometer presents quadratic relation with the spin frequency as expected. Subsequently, the value of K_{io} is deduced by fitting with (7). The fitted K_{io} fluctuates with differing uncertainties, but always within 30 mg/g^2, as given in Fig. 13(b). The uncertainty of K_{io} is consistent with the errors summarized in Table I. As the dominant error source, the tilt drift displayed in Fig. 9 could be used to interpret the detailed difference between different sets of test exemplified by Fig. 13. The up-and-down of the curve offset about one hundred of ng is reflected as different fitting values of coefficient C in (7). It is largely due to the difference in the average tilt among segments of 2.25 h as shown in Fig. 9. The slight variations in the curve shape are attributed to the variations in the tilt drift trend from segment to segment. The shape variations are then related to the dispersed linear coefficient B and quadratic coefficient A in (7), thus ultimately resulting in the uncertainty of K_{io}.

We have scrutinized the statistical characteristics of the K_{io} error induced by the tilt drift of the spin axis, based on fitting the randomly segmented data of 2.25 h in Fig. 9. As shown in Fig. 14, the statistical histogram of the influence on K_{io} follows a rule of Gaussian distribution with the deviation of 12 mg/g^2 within 1σ confidence interval in general. Hence,

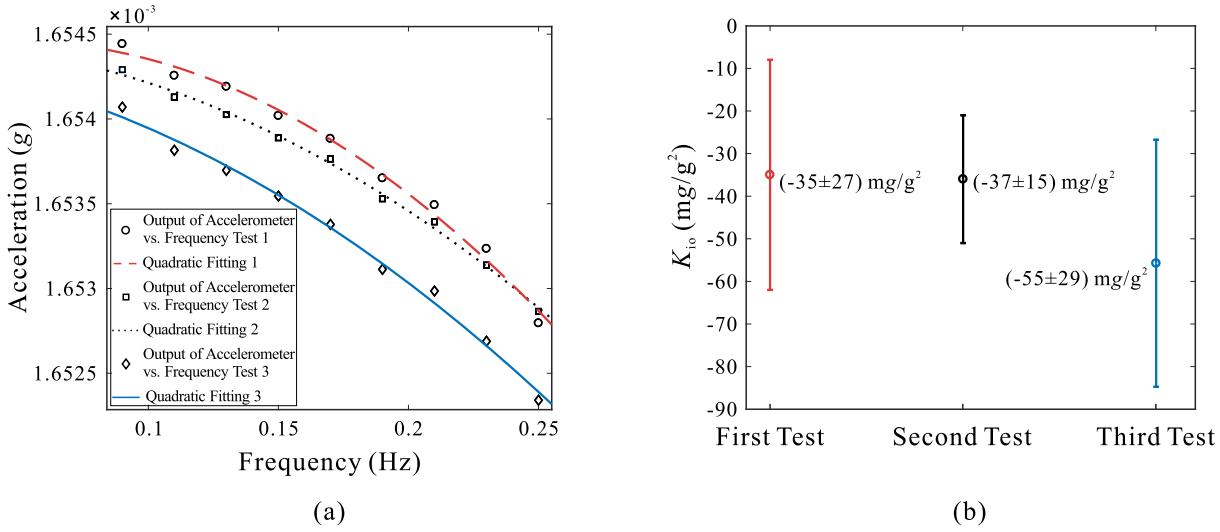

Fig. 13. Demodulated output of the accelerometer as a function of the rotation frequency (a) experimental results of three sets, respectively, denoted by circles, squares, and rhombuses, and fitting results plotted as curves, and (b) deduced results and uncertainties of K_{io}.

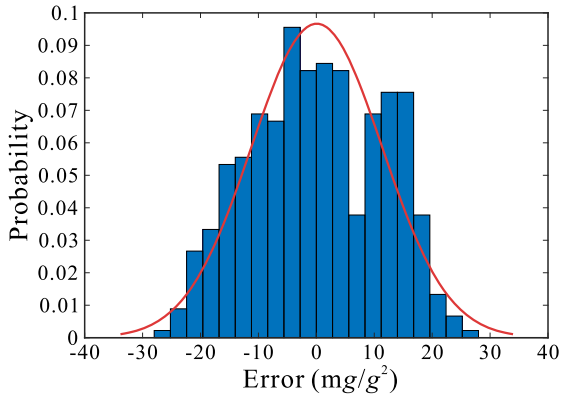

Fig. 14. Statistical histogram of the error caused by the tilt drift.

the experimental uncertainty related to tilt drift could be narrowed down using the weighted average method to treat the results of many measurements. Under the same conditions, the weight of each set is inversely proportional to its corresponding variance. For a series of test results, $K_{\mathrm{io1}} \pm u_1$, $K_{\mathrm{io2}} \pm u_2, \ldots, K_{\mathrm{io}j} \pm u_j, \ldots, K_{\mathrm{io}n} \pm u_n$, the weights for each test conform to

$$p_1 : p_2 : \cdots : p_n = \frac{1}{u_1^2} : \frac{1}{u_2^2} : \cdots : \frac{1}{u_n^2}. \tag{14}$$

The normalized relative weight for each measurement is

$$p_j = \frac{u_j^{-2}}{\sum_j^n u_j^{-2}}. \tag{15}$$

Based on the relative weights, we can obtain the final weighted average as

$$K_{\mathrm{io}} = p_1 K_{\mathrm{io1}} + p_2 K_{\mathrm{io2}} + \cdots + p_n K_{\mathrm{io}n}. \tag{16}$$

Then, the uncertainty can be written as

$$u = \sqrt{\frac{\sum_j^n p_j u_j^2}{(n-1)\sum_j^n p_j}}. \tag{17}$$

Substituting (15) into (17), the simplified uncertainty can be expressed as

$$u = \sqrt{\frac{n}{n-1}} \left(\sum_j^n u_j^{-2} \right)^{-1/2}. \tag{18}$$

Based on this data treatment method, the averaged value of K_{io} is derived to be -32 mg/g^2 and the uncertainty related to the tilt drift is updated to be 7.1 mg/g^2 by weighted averaging over more than ten sets of test. According to Table I, the errors from phase misalignment of demodulation, rotation stability of rate table, and response on acceleration frequency contain recognized systematic effects, which can be used to correct the measured value of K_{io}. After correction, the average of K_{io} is -34 mg/g^2. Taking into account all the other uncertainties besides the updated one for tilt drift in Table I, the combined uncertainty is calculated to be 8 mg/g^2. Therefore, the cross-coupling coefficient K_{io} is finally estimated to be (-34 ± 8) mg/g^2.

For comparison, the same accelerometer was calibrated by a static 12 points test on a tilted dividing head according to the scheme shown in Fig. 1. The cross-coupling coefficient of the nano-g accelerometer was calibrated to be $K_{\mathrm{io}} = (-85 \pm 88)$ mg/g^2 for a single test lasing $\sim$1 h. The test result is coincident with the one calibrated by the proposed dynamic approach within experimental uncertainties, whereas the uncertainty of the static calibration is marginally larger than the magnitude of its own average value. In contrast, the uncertainty of the static method close to 100 mg/g^2 is remarkably larger than the largest possible uncertainty of 30 mg/g^2 using the dynamic method, for one single set of tests. Further analysis shows that the bias drift of ± 5 μg during the static test duration bears the responsibility for the relatively large uncertainty. In comparison to the conventional procedure, the rotation modulation method is basically immune from the issue of slow bias drift while mostly limited by the tilt drift of the spin axis.

V. Conclusion

In this article, based on sequential rotation modulating the applied acceleration with discrete frequencies on a tilted rate table in the local gravity field, the cross-coupling coefficients of the accelerometer have been separated after systematically evaluating the error sources. K_{io} of a home-made accelerometer is determined with an uncertainty of 8 mg/g^2. In comparison to a static method of 12 discrete angular rotation on a tilted dividing head, this method demonstrates an improved uncertainty and robustness against the low-frequency bias drift of the sensor. A further improvement would be immediately achieved by suppressing the influence of the tilt drift. Among the error sources for tilt drift, the regular tidal tilt could be corrected to a great extent, and the irregular tilt drift of the spin axis might be monitored in real-time or alleviated by improving the performance of the rate table. K_{ip} could also be measured through the same procedure by simply mounting the accelerometer with the configuration that the PA is parallel to the rate table radius. This article helps complete the procedure of calibrating the cross-coupling coefficients of nano-g accelerometers. Especially for those dedicated to dynamic applications, their performance at an ultralow frequency close to dc not necessarily sustains to be excellent. This method would show superiority when testing them. It can also be applied to investigating the frequency dependence of cross-coupling coefficients in the low-frequency range.

Acknowledgment

The authors thank Prof. Wen He from the Institute of Manufacturing Technology and Automation, Zhejiang University, Hangzhou, China, for his help in the frequency-sweeping calibration test and Prof. Xueming Dong from the Changcheng Institute of Metrology & Measurement, Beijing, China, for discussion on precision centrifuge testing.

References

[1] W. Tian, S. C. Wu, Z. B. Zhou, S. B. Qu, Y. Z. Bai, and J. Luo, "High resolution space quartz-flexure accelerometer based on capacitive sensing and electrostatic control technology," *Rev. Sci. Instrum.*, vol. 83, no. 9, Sep. 2012, Art. no. 095002.

[2] W. Wu *et al.*, "High-sensitivity encoder-like micro area-changed capacitive transducer for a nano-g micro accelerometer," *Sensors*, vol. 17, no. 9, p. 2158, Sep. 2017.

[3] R. P. Middlemiss, A. Samarelli, D. J. Paul, J. Hough, S. Rowan, and G. D. Hammond, "Measurement of the Earth tides with a MEMS gravimeter," *Nature*, vol. 531, no. 7596, pp. 614–617, Mar. 2016.

[4] H. Liu and W. T. Pike, "A micromachined angular-acceleration sensor for geophysical applications," *Appl. Phys. Lett.*, vol. 109, no. 17, Oct. 2016, Art. no. 173506.

[5] H. Liu, W. T. Pike, C. Charalambous, and A. E. Stott, "Passive method for reducing temperature sensitivity of a microelectromechanical seismic accelerometer for marsquake monitoring below 1 nano-g," *Phys. Rev. A, Gen. Phys. Appl.*, vol. 12, no. 6, Dec. 2019, Art. no. 064057.

[6] Z. Li, W. Wu, P. Zheng, J. Liu, J. Fan, and L. Tu, "Novel capacitive sensing system design of a microelectromechanical systems accelerometer for gravity measurement applications," *Micromachines*, vol. 7, no. 9, p. 167, Sep. 2016.

[7] Y. Ma, Y.-Z. Bai, H.-Y. Li, Z.-B. Zhou, and Z. Zhou, "Identification and compensation of quadratic terms of a space electrostatic accelerometer," *Rev. Sci. Instrum.*, vol. 89, no. 11, Nov. 2018, Art. no. 114502.

[8] R. C. Blanchard, J. Y. Nicholson, J. R. Ritter, and K. T. Larman, "Orbital acceleration research experiment–calibration measurements," *J. Spacecraft Rockets*, vol. 32, no. 4, pp. 619–626, Jul. 1995.

[9] Y. Du, G. Gao, and T. Li, "A novel method for testing accelerometer transverse sensitivity," *Rev. Sci. Instrum.*, vol. 89, no. 12, Dec. 2018, Art. no. 125003.

[10] X. Huang, Z. Deng, Y. Xie, Z. Li, J. Fan, and L. Tu, "A new scale factor adjustment method for magnetic force feedback accelerometer," *Sensors*, vol. 17, no. 11, p. 2471, Oct. 2017.

[11] A. V. Veryaskin, *Gravity, Magnetic and Electromagnetic Gradiometry: Strategic Technologies in the 21st Century*. San Rafael, CA, USA: Morgan & Claypool, 2018.

[12] N. Kacem, S. Hentz, D. Pinto, B. Reig, and V. Nguyen, "Nonlinear dynamics of nanomechanical beam resonators: Improving the performance of NEMS-based sensors," *Nanotechnology*, vol. 20, no. 27, Jul. 2009, Art. no. 275501.

[13] *IEEE Standard Specification Format Guide and Test Procedure for Linear, Single-Axis, Nongyroscopic Accelerometers*, Standard IEEE Standard 1293TM-2018, Institute of Electrical and Electronics Engineers, Oct. 2008.

[14] P. Aggarwal, Z. Syed, X. Niu, and N. El-Sheimy, "A standard testing and calibration procedure for low cost MEMS inertial sensors and units," *J. Navigat.*, vol. 61, no. 2, pp. 323–336, Apr. 2008.

[15] Z. F. Syed, P. Aggarwal, C. Goodall, X. Niu, and N. El-Sheimy, "A new multi-position calibration method for MEMS inertial navigation systems," *Meas. Sci. Technol.*, vol. 18, no. 7, pp. 1897–1907, Jul. 2007.

[16] G. A. Aydemir and A. Saranlı, "Characterization and calibration of MEMS inertial sensors for state and parameter estimation applications," *Measurement*, vol. 45, no. 5, pp. 1210–1225, Jun. 2012.

[17] I. Frosio, F. Pedersini, and N. A. Borghese, "Autocalibration of MEMS accelerometers," *IEEE Trans. Instrum. Meas.*, vol. 58, no. 6, pp. 2034–2041, Jun. 2009.

[18] S.-Q. Ren, Q.-B. Liu, M. Zeng, and C.-H. Wang, "Calibration method of accelerometer's high-order error model coefficients on precision centrifuge," *IEEE Trans. Instrum. Meas.*, vol. 69, no. 5, pp. 2277–2286, May 2020.

[19] H. Sohrabi and S. Ebadollahi, "Accuracy enhancement of MEMS accelerometer by determining its nonlinear coefficients using centrifuge test," *Measurement*, vol. 112, pp. 29–37, Dec. 2017.

[20] C. Sun, S.-Q. Ren, and C.-H. Wang, "Revised error calibration model of linear accelerometer on precision centrifuge," *Rev. Sci. Instrum.*, vol. 90, no. 8, Aug. 2019, Art. no. 085002.

[21] S. Wang and S. Ren, "Calibration of cross quadratic term of gyro accelerometer on centrifuge and error analysis," *Aerosp. Sci. Technol.*, vol. 43, pp. 30–36, Jun. 2015.

[22] D. Capriglione *et al.*, "Development of a test plan and a testbed for performance analysis of MEMS-based IMUs under vibration conditions," *Measurement*, vol. 158, Jul. 2020, Art. no. 107734.

[23] G. P. Ripper, R. S. Dias, and G. A. Garcia, "Primary accelerometer calibration problems due to vibration exciters," *Measurement*, vol. 42, no. 9, pp. 1363–1369, Nov. 2009.

[24] T. Bruns and S. Gazioch, "Correction of shaker flatness deviations in very low frequency primary accelerometer calibration," *Metrologia*, vol. 53, no. 3, pp. 986–990, Jun. 2016.

[25] *IEEE Recommended Practice for Precision Centrifuge Testing of Linear Accelerometers*, Standard IEEE Standard 836-2009, Institute of Electrical and Electronics Engineers, Sep. 2009.

[26] T. Y. Liu, S. Y. Wang, F. T. Han, and Q. P. Wu, "Modeling and compensation of cross-axis coupling in an electrostatic accelerometer for testing the equivalence principle," *Rev. Sci. Instrum.*, vol. 89, no. 12, Dec. 2018, Art. no. 124501.

[27] M. Yu, T. Cai, L. Tu, C. Hu, and L. Yu, "Posterror compensation of moving-base rotating accelerometer gravity gradiometer," *IEEE Trans. Instrum. Meas.*, vol. 70, Jul. 2020, Art. no. 9500410.

[28] E. Wielandt and M. Zumberge, "Measuring seismometer nonlinearity on a shake table," *Bull. Seismolog. Soc. Amer.*, vol. 103, no. 4, pp. 2247–2256, Aug. 2013.

[29] S. Cesare and G. Catastini, "Gradiometer on-orbit calibration procedure analysis," Thales Alenia Space, Cannes, France, Tech. Rep. GO-TN-AI-0069, 2008.

[30] B. Frommknecht, D. Lamarre, M. Meloni, A. Bigazzi, and R. Floberghagen, "GOCE level 1b data processing," *J. Geodesy*, vol. 85, no. 11, pp. 759–775, Nov. 2011.

[31] S. Yan, Y. Xie, M. Zhang, Z. Deng, and L. Tu, "A Subnano-g electrostatic force-rebalanced flexure accelerometer for gravity gradient instruments," *Sensors*, vol. 17, no. 11, p. 2669, Nov. 2017.

[32] W. Wu, J. Zhou, X. Liu, and L. Nie, "The method for the resolution test of accelerometer based on the double axis tilt method," *Geophys. Geochem. Explor.*, vol. 39, pp. 37–40, Dec. 2015.

[33] S. Wu, S. Fan, J. Luo, and H. Hsu, "Folded pendulum tiltmeter," *Rev. Sci. Instrum.*, vol. 73, no. 5, pp. 2150–2156, May 2002.

Mengqi Zhang received the B.S. degree in physics from Anhui University, Hefei, China, in 2016. She is currently pursuing the Ph.D. degree with the Huazhong University of Science and Technology (HUST), Wuhan, China.

Since 2016, she has been involved in calibration of nano-g inertial sensors. Her research interests include the dynamic response modeling, evaluation, and optimization of high-resolution inertial sensors.

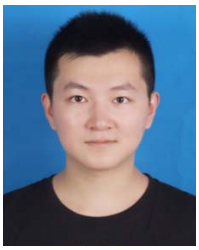

Shitao Yan received the B.Eng. degree in electronic science and technology and the Ph.D. degree in precision measurement physics from the Huazhong University of Science and Technology (HUST), Wuhan, China, in 2013 and 2018, respectively.

He is currently a Post-Doctoral Researcher with the School of Physics, HUST. His research interests include inertial sensors, capacitive transducers, weak signal detection, and gravity gradient measurement.

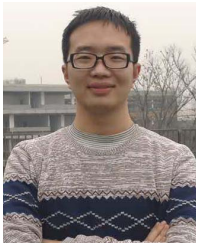

Zhongguang Deng received the B.S. degree in physics from the Huazhong University of Science and Technology (HUST), Wuhan, China, in 2015.

His current research interests include gravity measurement technologies, precise measurement of physics, and gravity sensors.

Peng Chen received the B.S. degree from the School of Physics, Huazhong University of Science and Technology (HUST), Wuhan, China, in 2016, where he is currently pursuing the Ph.D. degree.

His research interests include signal processing, system modeling, inertial sensor technology, and gravity gradiometer.

Zhi Li received the B.S. degree in material physics from the Wuhan University of Science and Technology, Wuhan, China, in 2017. He is currently pursuing the Ph.D. degree with the School of Physics, Huazhong University of Science and Technology (HUST), Wuhan.

His research interests include mathematical modeling of accelerometer, vibration test and calibration, data processing, and analysis.

Ji Fan received the B.S. degree in engineering from the Wuhan Institute of Science and Technology, Wuhan, China, in 2001, and the M.S. and Ph.D. degrees in microelectronic engineering from the University of Limoges, Limoges, France, in 2005 and 2009, respectively.

From 2010 to 2012, he was a Research Fellow with Nanyang Technological University, Singapore, where his research interests were MEMS fabrication and 3-D integration technology via bonding. He joined the Huazhong University of Science and Technology (HUST), Wuhan, in 2013, as an Associate Professor. His current research interests include semiconductor process technology, MEMS, and gravity gradient measurement.

Huafeng Liu received the M.Sc. degree in MEMS from the University of Southampton, Southampton, U.K., in 2011, and the Ph.D. degree in MEMS from Imperial College London, London, U.K., in 2016.

He has been working as an Associate Professor of MEMS with the School of Physics, Huazhong University of Science and Technology (HUST), Wuhan, China, since 2017. He has authored or coauthored over 50 peer-reviewed research articles and a book chapter, and holds over ten patents. His major research interests include the design, fabrication, and characterization of high-performance MEMS sensors.

Dr. Liu won the MINE2020 Young Scientist Award.

Jinquan Liu received the B.Sc. degree in physics from Peking University, Beijing, China, in 1997, the M.Sc. degree in optical physics from the Institute of Physics, Chinese Academy of Sciences, Beijing, in 2000, and the Ph.D. degree in nanophotonics from the Swiss Federal Institute of Technology, Lausanne, Switzerland, in 2007.

He worked as a Post-Doctoral Researcher with the Max Planck Institute of Microstructure Physics, Halle, Germany, in 2008, and with the Swiss Federal Laboratories for Materials Testing and Research, Thun, Switzerland, in 2009, respectively. He has been working on high-precision acceleration measurement as an Associate Professor with the School of Physics, Huazhong University of Science and Technology (HUST), Wuhan, China, since 2010.

Liangcheng Tu received the B.S. degree from Hubei University, Wuhan, China, in 1996, and the Ph.D. degree from the Huazhong University of Science and Technology (HUST), Wuhan, in 2006, all in physical science.

He is currently a Full-Time Professor with the School of Physics and Astronomy, Sun Yat-sen University, Zhuhai, China, and a part-time Professor with the School of Physics, HUST. His current research interests include laboratory gravitational experiments, gravity measurement technologies, and semiconductor device physics.